PAPER

Check for updates

Vapor phase synthesis of metal–organic frameworks on a nanofibrous aerogel creates enhanced functionality†

Vahid Rahmanian, [ID] Muhammed Ziauddin Ahmad Ebrahim, [ID] Seyedamin Razavi, Mai Abdelmigeed, Eduardo Barbieri, Stefano Menegatti, [ID] Gregory N. Parsons, [ID] Fanxing Li, [ID] Tahira Pirzada [ID] * and Saad A. Khan [ID] *

This study introduces an innovative approach for synthesizing metal–organic frameworks (MOFs) on 3D-structured hierarchically porous nanofibrous aerogels (NFAs). The NFA was initially fabricated by solid-templating cellulose diacetate (CDA)–silica electrospun nanofibers and subsequently coated with ZIF-8 MOF *via* vapor phase synthesis. The ZIF-8 MOF – known for its CO_2 adsorption, heavy metal removal, and antibacterial properties – was synthesized directly on the NFA, producing a uniform layer of densely packed ZIF-8 crystals on the CDA–silica nanofibers. The integrated MOF–NFA features a rich functional diversity. First, measurements of mechanical compressibility demonstrated the robustness and strain recovery of the CDA–silica@ZIF-8 NFAs, and thus their applicability in environments that entail exposure to mechanical stress. Furthermore, the ZIF-8-coated aerogel, with its high CO_2 adsorption rate and capacity (4.04 mmol g^{-1}), holds promise as a substrate for CO_2 separation or sequestration. The aerogel also exhibits excellent performance in removing heavy metals, particularly Cu(II) ions (>99% removal). The high adsorption capacity is rooted in the thin and uniform ZIF-8 coating of the NFA, and grants applicability for water purification. The antibacterial properties of the hybrid aerogel demonstrate efficacy against both Gram-negative and Gram-positive bacteria. In summary, the hybrid NFA shows promise for various applications, particularly in tackling challenges in environmental and biomedical fields, encompassing sorption, catalysis, filtration, water purification, and antimicrobial applications.

1. Introduction

Metal–organic frameworks (MOFs) are a class of crystalline porous coordination polymers composed of metal ions and organic linkers. These materials exhibit high crystallinity and thermal stability,[1] and their large specific surface area makes them attractive substrates for water purification,[2] drug delivery,[3] gas storage,[4] separation,[5] catalysis,[5] sensing[6] and energy storage.[7,8] In their native form of powders or colloidal crystals, however, MOFs display limited processability.[9,10] Additionally, their intrinsic micro/meso-porosity can limit the access and diffusion kinetics of large molecules and nanomaterials.[11] The integration of MOFs with various substrates represents a versatile and cost-effective route to increase their formability and enhance their adsorptive behavior. In this context, recent approaches focused on depositing layers of MOF crystals on fibers, inorganic particles, and nanosheets *via* layer-by-layer,[12] spray[13] and *in situ* growth methods.[10,14,15] These methods,

however, are often limited by the roughness, surface wettability, and functionality of the matrix, and require surface modification to increase the compatibility between the MOF layer and the substrate.[16–18] MOF crystals were also embedded into hollow fibers,[19] electrospun micro and nanofiber mats,[20] and polymer films[21,22] to prepare composite membranes. However, particle aggregation and the poor interaction between the MOF particles and the polymer matrix resulted in low MOF contents and thus low specific surface areas.[9]

3D self-supported aerogels have recently emerged as excellent candidates for the synthesis of MOF composite materials owing to their innate hierarchical porosity and surface area.[23,24] Hybrid MOF-aerogels have been fabricated by growing or aggregating MOF particles on aerogel networks *via* either simple mixing, solvothermal synthesis, or high-internal-phase emulsion.[23–28] Early MOF-loaded aerogels, prepared by mixing MOF nanoparticles in a dispersion of (bio)polymers, followed by gelation and freeze-drying, relied on relatively weak interactions (*e.g.*, physical entanglement and van der Waals forces) and suffered from limited stability.[24,25] Other MOF-aerogels were fabricated *via in situ* synthesis of MOFs on the surface of aerogel precursors, followed by gelation, solvent exchange, and freeze-drying – a process known as solvothermal approach, which is

Department of Chemical & Biomolecular Engineering, North Carolina State University, Raleigh, NC 27695-7905, USA. E-mail: tpirzad@ncsu.edu; khan@eos.ncsu.edu

† Electronic supplementary information (ESI) available. See DOI: https://doi.org/10.1039/d3ta05299k

considerably more laborious and provides networks with inadequate structural integrity.[9,26,29,30] Hybrid MOF aerogels have also been fabricated *via* high-internal-phase emulsion (HIPE), which consists of synthesizing MOFs on the interface of Pickering particles followed by freeze-drying.[27] This procedure, however, is challenging due to the instability of 3D Pickering emulsion architectures during MOF synthesis. Notably, these methods relied on MOF integration into conventional aerogels, which requires precise tuning of fabrication conditions to achieve gelation over crystallization and precipitation, thus limiting their applicability to a narrow range of pore apertures, porosities, and densities.[31] Furthermore, irregular agglomeration of MOF particles decreases the specific surface area of the coat, thus limiting the functionality of the hybrids.[32] These limitations highlight the need for a robust and sustainable fabrication method that affords durable integration of MOF particles on aerogels' interconnected networks.

Nanofibrous aerogels (NFAs) are a young family of highly porous and ultra-light self-supported materials composed of a 3D network of interconnected nanofibers.[33–35] These fibrous networks provide a mechanically robust substrate with a higher surface area compared to conventional aerogels.[35–38] NFA fabrication *via* freeze-drying of a dispersion of short electrospun nanofibers in a non-solvent produces a fibrous entanglement featuring a bimodal distribution of primary (4–7 µm wide) and secondary pores (40–60 µm diameter).[34,39] Compared to the laborious and expensive synthesis of conventional aerogels, this efficient method has allowed researchers to broaden the landscape of NFAs' functionality. Among hybrid NFAs, thermally treated cellulose diacetate (CDA)–silica has received considerable attention for its excellent thermal and mechanical stability, sustainability, flexibility, formability, and hierarchical porosity.[35] The addition of a small amount of silica to CDA chains followed by thermal treatment affords a robust 3D structure, with strong bonding between fibers. Notably, CDA–silica NFAs can sustain significant deformations under high compressive strains (>80%) without collapse, which has been attributed to the hierarchical cellular structure of the aerogel, consisting of flexible walls made of densely entangled nanofibers.[35] Furthermore, the CDA–silica nanofibers feature high specific surface area, ideal for the formation, growth, or attachment of MOF crystals.

In this study, we synthesized MOF crystals directly on 3D self-supported, ultralight CDA–silica NFA. Unlike conventional aerogels, our NFAs are prepared *via* a straightforward solid templating approach without involving time-consuming processing steps and large amounts of organic solvents. We adopted ZIF-8, a member of the zeolitic imidazolate framework family, as model MOF to deposit on the NFA. Our fabrication approach consists of depositing thin layers of zinc oxide (ZnO) on the CDA–silica NFA substrate *via* atomic layer deposition (ALD) followed by converting ZnO to ZIF-8 by treatment with organic vapors of 2-methylimidazole (2-MeIm) linker. Vapor phase synthesis of MOFs has several advantages over traditional solution-phase solvothermal synthesis, such as higher yield, lower cost and environmental impact, and broader functional outcomes.[40–42] Recent efforts in developing solvent-free

MOF synthesis – including chemical vapor deposition (CVD), ALD, molecular layer deposition (MLD), and combined physical vapor deposition-CVD, have focused on depositing MOF thin films on 2D substrates.[43]

Studies combining vapor phase MOF synthesis with 3D substrates remain largely unexplored, with the beauty of our approach being to preserve the high micro/meso-porosity of ZIF-8 crystals while combining it with the hierarchical porosities, flexibility, formability, and low density of NFAs. The distinctive combination of sol–gel electrospinning, aerogel fabrication and vapor phase MOF synthesis creates a sustainable and potentially scalable platform for superior performance of ZIF-8 powders in a multitude of applications. The uniqueness of this study lies in (a) the fabrication MOF–nanofibrous aerogels, in particular the use of a solvent-free approach to create MOFs on the nanofibrous surface of the aerogels. Such surface decoration results in firmly attached MOF particles and enhances access to the MOF, (b) the use of nanofibrous instead of conventional aerogels in MOF incorporation wherein the NFA requires fewer steps and provides enhanced functionalities, (c) the mechanical robustness of our systems, possibly resulting from the nanofibrous structure of the aerogels and fabrication protocols; and, (d) multifunctional performance the hybrid NFAs offer. Our proof of concept results on CO_2 capture, antibacterial properties and heavy metal removal highlight the versatility of our system. Nevertheless, they are by no means comprehensive and future studies need to be undertaken to delve into each of these further.

2. Result and discussion

2.1 Construction, morphology and characterization

We synthesized NFAs by freeze-drying a dispersion of hybrid CDA–silica nanofibers following our previously established protocol.[35] Briefly, the initial step involves sol–gel electrospinning of bead-free hybrid CDA–silica nanofibers under controlled process conditions and precursor mixture composition. The resulting 3D self-supported CDA–silica NFA is generated by chopping the nonwoven electrospun nanofibers into short fibers of specific aspect ratios in tertiary butanol (*t*-BuOH, a nonsolvent), followed by freeze-drying and thermal treatment. Freeze-drying leads to the creation of a hierarchical cellular structure due to the concentration of entangled fiber fragments between growing solvent crystals. Then, the NFA is conformally coated with thin layers of ZnO using an ALD process. Fig. S2c† shows the scanning electron microscope (SEM) of the ZnO coated NFAs with the hierarchical porosity. Finally, the ZnO is converted to ZIF-8 to create CDA–silica@ZIF-8, by hanging ZnO-decorated CDA–silica NFA in a closed glass jar containing a powder bed of 2-MeIm for 6 hours at 135 °C under vapor phase conversion conditions (schematic in Fig. 1). This process results in a densely packed, uniformly distributed layer of ZIF-8 crystals to the NFA substrate. The hierarchical porous structure of the NFA facilitates diffusion and access to the active sites located within ZIF-8 micro/mesopores.

As anticipated, the ZnO-coated CDA–silica NFA substrate enables the creation of a uniform and conformal layer of the

Fig. 1 Pathway toward fabrication of CDA−silica@ZIF-8 NFA.

metal oxide for ZnO-to-ZIF-8 conversion, while also serving as an adhesion layer between ZIF-8 and the NFA substrate. The morphology of CDA−silica nanofibers and NFA coated with ZIF-8 crystals is presented in Fig. 2. As shown by SEM images, the

ZIF-8 crystals are tightly packed, uniformly distributed, and appear to be strongly attached to the fiber surface coated with 60 (Fig. 2a and b) and 120 (Fig. 2d and e) cycles of ZnO ALD. The morphology of pristine CDA−silica NFA demonstrated in Fig. 2c

Fig. 2 Morphology and characterization of CDA−silica@ZIF8 hybrid: (a and b) SEM images of CDA−silica@ZIF8-60cy at two magnifications. (c) SEM image of pristine CDA−silica NFA. (d and e) SEM image of CDA−silica@ZIF8-120cy at two magnifications. (f) SEM image showing the porous structure of CDA−silica@ZIF8-120cy. (g) XRD patterns of CDA−silica, CDA−silica@ZnO, CDA−silica@ZIF8-60cy and simulated ZIF-8 powder. (h) N_2 physisorption isotherms of CDA−silica, CDA−silica@ZnO-60cy, CDA−silica@ZnO-120cy, CDA−silica@ZIF8-60cy and CDA−silica@ZIF8-120cy NFAs at 77 K. (i) BET specific surface area calculated form N_2 physisorption isotherms.

shows the hierarchical porous structure consisting of secondary and primary pores and is retained after the growth of ZIF-8 (Fig. 2f). Video S1† demonstrates qualitatively that the ZIF-8 crystals remain firmly attached to the NFA substrate without detachment following mechanical deformation. Additionally, Energy Dispersive X-ray (EDX) mapping displayed in Fig. S1† confirms the uniform distribution of zinc and nitrogen in the ZIF-8 decorated CDA–silica nanofibers. This level of homogeneity indicates a high conversion rate of ZnO to ZIF-8 crystals, which is desirable in our approach. As demonstrated in SEM images shown in Fig. 2, coating nanofibers with 60 and 120 ZnO ALD cycles resulted in crystallization of ZIF-8 during vapor phase synthesis. In order to investigate the impact of different numbers of ZnO ALD cycles on the crystallization of ZIF-8, we investigated the vapor phase synthesis on nanofibers coated with 200 and 300 ZnO ALD cycles. The SEM images in Fig. S2† illustrate the agglomeration of ZIF-8 crystals on the fiber surface for both the 200 (Fig. S2a†) and 300 (Fig. S2b†) cycles of ZnO ALD. This resulted in a decrease in mechanical properties, rendering the nanofibers brittle.

To further evaluate the presence of ZIF-8 crystals on CDA–silica NFA, we conducted a comparison of XRD between CDA–silica, ZnO coated CDA–silica and CDA–silica@ZIF-8 NFAs. As shown in Fig. 2g, the XRD of the CDA–silica@ZIF-8 NFA with 60 cycles of ZnO ALD and 6 hours of conversion displayed characteristic diffraction peaks at 2θ values of 7.3°, 10.4°, 12.8°, 14.7°, 16.5° and 18.1°, which correspond to the (110), (200), (211), (220), (013) and (222) crystal faces of ZIF-8, indicating successful conversion of the ZnO to ZIF-8 crystals during vapor phase conversion. The peak broadening observed in the sample XRD pattern suggests the formation of nanosized crystals. The crystallite size was calculated to be approximately ~80–120 nm using the Scherrer equation.[44] This observation supports the role of hierarchical morphology of the NFA as well as the nanoscale diameter of the nanofibers in facilitating the formation of smaller crystals on the substrate and promoting the distribution of ZIF-8 crystals. FTIR spectroscopy was also performed and revealed characteristic IR peaks at 1574 cm^{-1}, 1146 cm^{-1}, 758 cm^{-1}, and 420 cm^{-1}, corresponding to aromatic C=N, C–N, out-of-plane bending of the 2-MeIm ring, and Zn–N stretching modes of ZIF-8, respectively (Fig. S3a†).

Later we determined the surface area of pristine CDA–silica, CDA–silica@ZnO, and CDA–silica@ZIF-8 under different conditions, using the Brunauer–Emmett–Teller (BET) method (Fig. 2h). The results further prove that the vapor phase synthesis of ZIF-8 was successful, as the surface area of the CDA–silica@ZIF-8 composites increases to 325 and 420 m^2 g^{-1} for 60 and 120 ZnO ALD cycles respectively compared to 7.8 m^2 g^{-1} for bare CDA–silica NFA. Furthermore, the pore size distribution of the CDA–silica@ZIF-8 composites was determined using the BET method, as depicted in Fig. S2b.† The pore sizes of the ZIF-8 component of the composites range from 8 to 11 Å, aligning closely with values reported in the literature.[45,46] The micro/mesoporosity of the ZIF-8 crystals is responsible for the high specific surface area observed in the CDA–silica@ZIF-8 composites. However, when the number of ZnO ALD cycles is further increased to 200 and 300, the surface area decreases to

264 and 160 m^2 g^{-1}, respectively. This indicates that pore blockage, agglomeration (as illustrated in the SEM images in Fig. S2a and b†) or degradation of the MOF crystals may have occurred due to the presence of clustered granules contributed by 2-MeIm. Based on all the findings from the characterization analysis, we have determined that maintaining the number of ZnO ALD cycles at 60 and 120 is the most suitable approach for vapor phase conversion of ZnO to ZIF-8. These specific ZnO ALD cycle numbers consistently yield uniformly distributed ZIF-8 crystals with a significantly high specific surface area.

2.2 Mechanical properties

Mechanical properties of the NFAs are attributed to their robust hierarchical cellular structure, which allows for significant deformations without fracture. Unlike conventional aerogels, the NFAs can withstand a compressive strain (ε) of up to 80% and recover their original volume after stress release.[34,35] To assess the compressibility, strength, and shape recovery of the NFAs, we conducted a series of compressive stress–strain (σ–ε) tests on CDA–silica and CDA–silica@ZIF-8 NFAs samples (details in the Experimental section). Fig. 3 shows compression–relaxation curves for the NFAs at set ε maxima of 10, 20, 40, 60, and 80%, revealing three characteristic deformation regimes: a Hookean or linear elastic regime at low strains, a plateau region representing elastic buckling of the cell walls, and a densification regime at higher strains with steeply increasing σ and dσ/dε. Both CDA–silica (Fig. 3a) and CDA–silica@ZIF-8 NFAs (Fig. 3b) exhibit a small Hookean region with an elastic modulus of 3.0 kPa. The similar Young's moduli of the two NFAs indicates that MOF synthesis has a small effect on their mechanical strength. CDA–silica@ZIF-8 NFA displays robust mechanical performance, sustaining large deformations without collapse at compressive strains up to 80% and exhibiting fatigue resistance after 50 stress–strain cycles at 60% strain (Fig. 3b and c). This resilience is attributed to the hierarchical cellular structure of flexible walls made of densely entangled nanofibers, which act as a cushion when compressed and bounce back to their original position after load removal.[34,35] The retention of 3D geometry after repeated compressive cycles in both cases indicates the role played by strong interactions developed during thermal treatment in making the 3D structure more robust and flexible to support multiple cycles of heavy loads with shape recovery. The strain is absorbed by the deformation of primary pores and beyond 60% strain by the densification of secondary pores. Strain-dependent hysteresis loops in most of the loading–unloading curves indicate energy dissipation due to the fibrous network. The small quantity of silica (~6 wt%) in the NFAs helps glue the CDA chains strong enough to hold the fibers together and develop a robust 3D structure upon heating.

The CDA–silica@ZIF-8 NFA exhibits a combination of unique properties, including ultralight weight, hierarchically porous structure including micro, meso and macroporosities, high specific surface area, and mechanical robustness. These distinctive characteristics make the CDA–silica@ZIF-8 NFAs highly versatile and suitable for an extensive array of
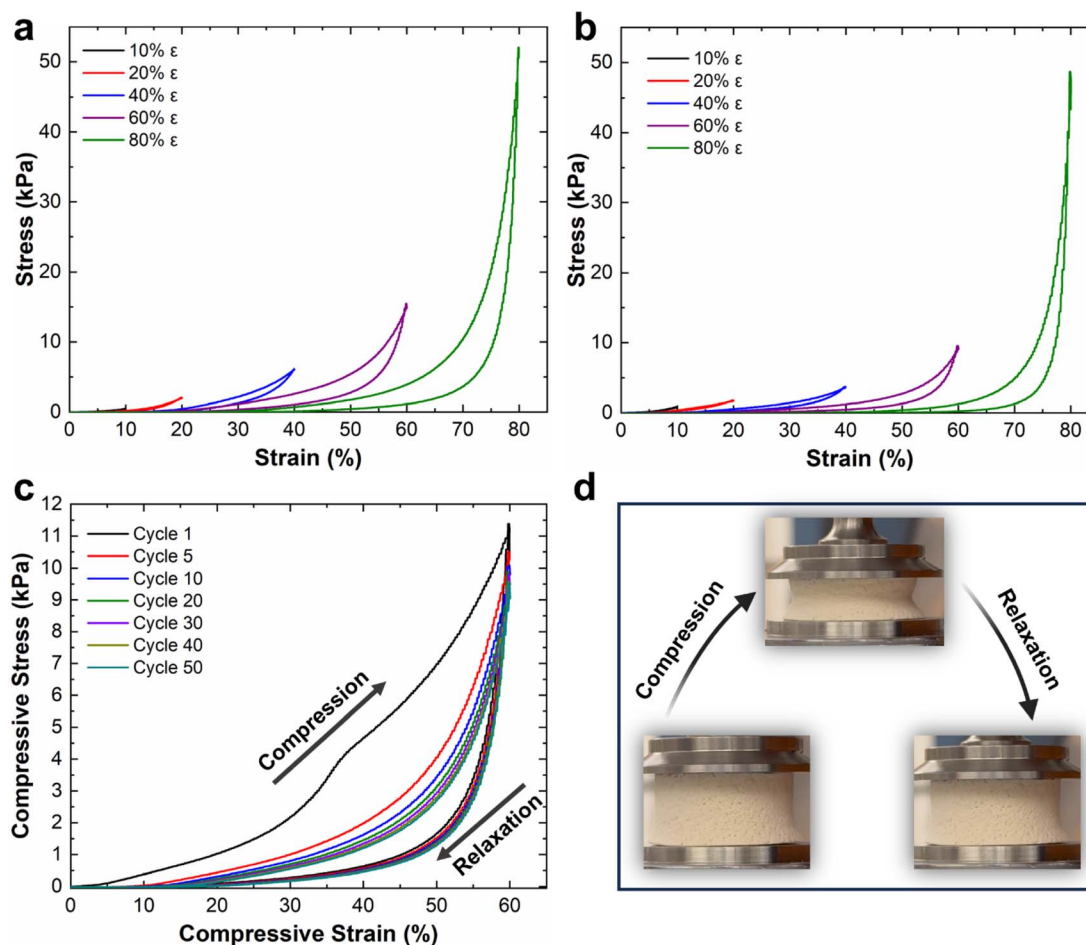
This journal is © The Royal Society of Chemistry 2024

J. Mater. Chem. A, 2024, **12**, 214–226 | **217**

Fig. 3 Compressive stress–strain experiments of (a) CDA–silica NFA, (b) CDA–silica@ZIF-8 NFA, (c) cyclic fatigue test of CDA–silica@ZIF-8 NFA at 60% strain for 50 cycles and (d) digital photograph of how the CDA–silica@ZIF-8 NFA changes under compressive deformation.

applications. Their ultralight nature enables efficient transport and handling, while the hierarchically porous structure facilitates enhanced mass transfer and adsorption capabilities. The high surface area of the NFAs provides ample active sites for various reactions and sorption processes. Additionally, their mechanical robustness ensures long-lasting performance under challenging conditions.

2.3 CO_2 adsorption

Thus far, our research has focused on the ZIF-8 vapor phase synthesis, morphology, characterization, and mechanical properties of CDA–silica@ZIF-8 NFA. In this and the following sections, we examine the functional attributes of our NFAs. We begin by investigating the ability of our hybrid NFA for application in carbon dioxide (CO_2) adsorption.

CO_2 adsorption is recognized as an efficient approach for mitigating excessive CO_2 emissions, which contribute to a range of ecological crises, including climate change, declining biodiversity, and glacial retreat.[47–50] ZIF-8 is a promising material for the separation and adsorption of CO_2 owing to its exceptional porous structure.[51] Loading it on the aerogel structure provides significant surface area and exposes active sites in the

micropores of ZIF-8, enabling the efficient adsorption of CO_2 molecules.[43] The thermal and chemical stability of ZIF-8 also makes it desirable for CO_2 adsorption and separation processes.[51] Finally, the pores within ZIF-8 can accommodate CO_2 gas by providing Langmuir sites, which can replace other gas molecules with CO_2 molecules (Fig. 4a).[52]

To evaluate the CO_2 adsorption capacity of CDA–silica@ZIF8-120cy and CDA–silica@ZIF8-60cy, a gravimetric approach was employed at 35, 60, and 80 °C. The TGA equipment was supplied with a mixture of CO_2/Ar (15/85%) as the inlet gas. The results showed that the amount of CO_2 adsorbed by both the NFAs, decreased with increasing temperature (Fig. 4b), as the adsorption process was exothermic. These materials exhibit fast adsorption rates, as evident from Fig. 4b and S4.† Both substances attained their maximum adsorption capacity within the first few minutes and reached equilibrium within ten minutes. Fig. 4b indicates that at a temperature of 35 °C, CDA–silica@ZIF8-120cy achieved 93.4% of its total adsorption within the first minute. The corresponding values at 60 °C and 80 °C were 86.7% and 90.9%, respectively. Similarly, for CDA–silica@ZIF8-60cy, the material achieved 82.6% of total adsorption at a temperature of 35 °C. The values for
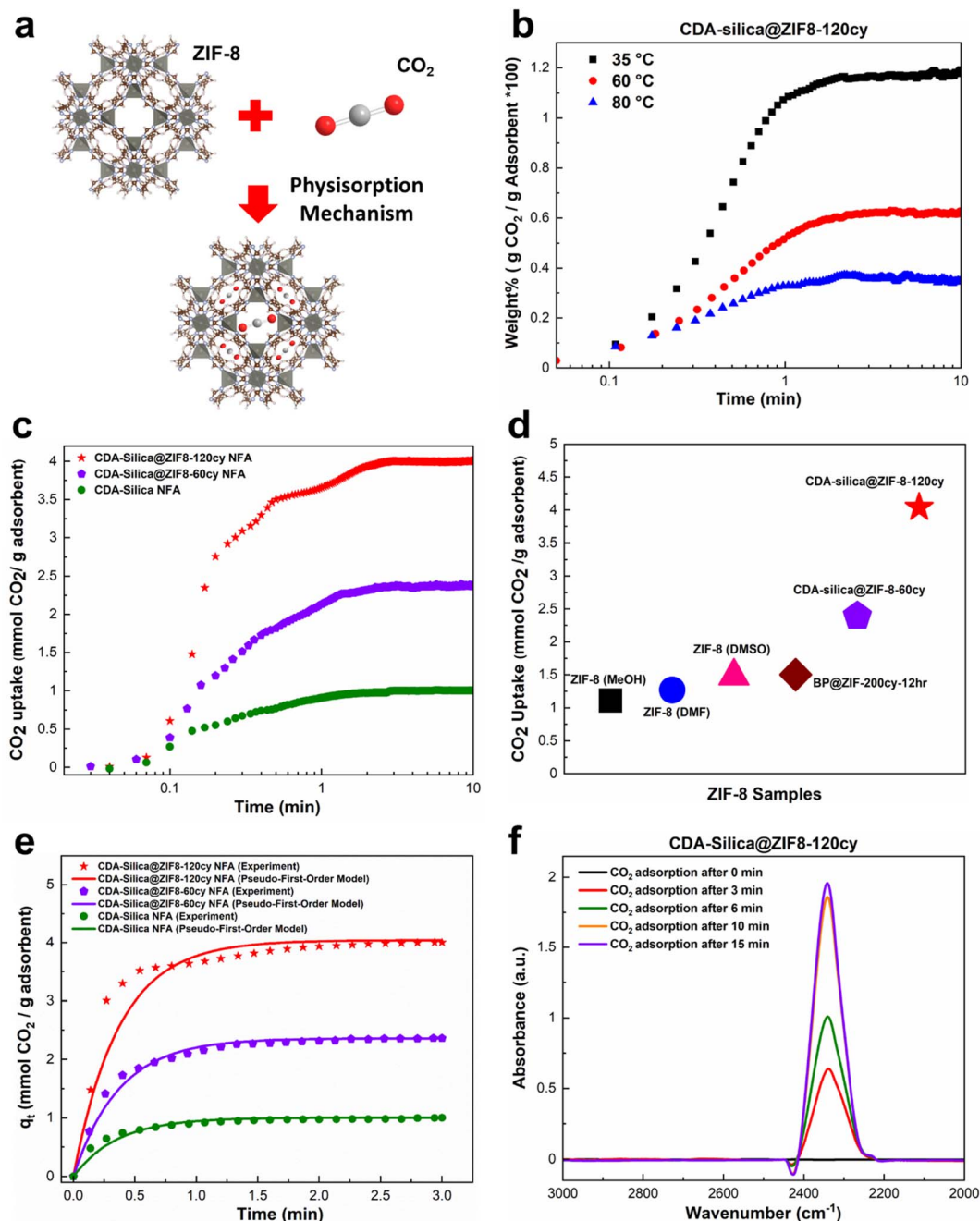
218 | *J. Mater. Chem. A*, 2024, **12**, 214–226

This journal is © The Royal Society of Chemistry 2024

Fig. 4 CO_2 adsorption capacity of CDA−silica@ZIF-8 NFA: (a) schematic illustration of CO_2 adsorption in ZIF-8 through physisorption mechanism, (b) CO_2 uptake of CDA−silica@ZIF8-120cy at 35, 60 and 80 °C from a mixture of 15% CO_2 and 85% Ar, (c) CO_2 uptake of CDA−silica@ZIF-8 NFA at 35 °C from a mixture of 90% CO_2 and 10% Ar, (d) CO_2 adsorption capacity of our CDA−silica@ZIF-8 NFA compared to other works,[43,53] (e) a comparison between the experimental and predicted CO_2 adsorption curves using the pseudo-first-order model for CDA−silica@ZIF8-120cy, CDA−silica@ZIF8-60cy and CDA−silica NFAs at an adsorption temperature of 35 °C. (f) *In situ* FTIR of CO_2 adsorbed on CDA−silica@ZIF8-120cy monitored as a function of time at 35 °C and 1 bar.

temperatures of 60 °C and 80 °C were 84.6% and 85.4%, respectively (Fig. S4†). Additionally, the cyclic stability of CDA–silica@ZIF8-120cy NFA was found to be consistent over 50 cycles as shown in Fig. S5,† suggesting the capability of these NFAs to remove CO_2 in a cyclic adsorption/desorption procedure without loss in sorption capacity. The experiments conducted with high concentrations of CO_2 (90% CO_2 and 10% Ar at 35 °C

and 1 bar) showed that the materials being tested exhibited excellent performance in terms of adsorption capacity and rate of adsorption, *i.e.*, CDA–silica@ZIF8-120cy and CDA–silica@ZIF8-60cy were able to adsorb 4.04 mmol g^{-1} and 2.39 mmol g^{-1}, respectively (Fig. 4c). The amount of CO_2 adsorbed on CDA–silica@ZIF8-120cy and CDA–silica@ZIF8-60cy was also found to be significantly higher than similar
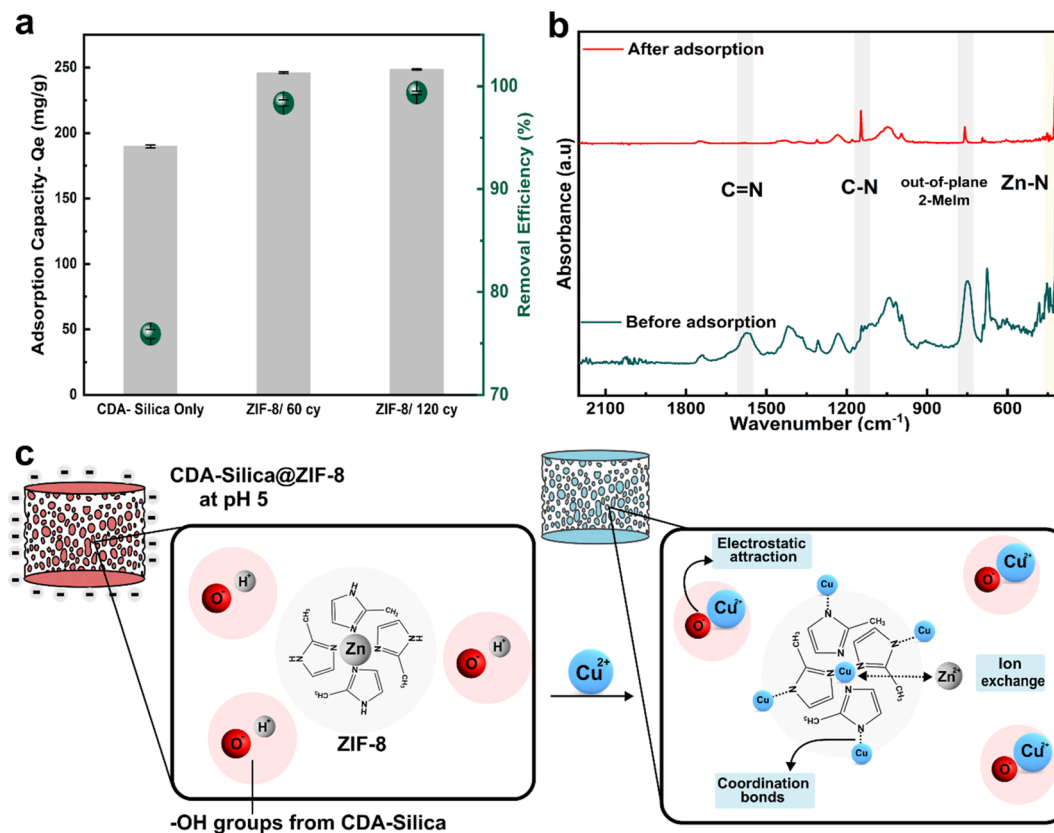
This journal is © The Royal Society of Chemistry 2024

J. Mater. Chem. A, 2024, **12**, 214–226 | **219**

Fig. 5 Heavy metal removal: (a) adsorption capacity (mg g^{-1}) and removal efficiency (green circles, %) for 20 mg of the adsorbent (aerogel) load in 100 mg L^{-1} of stock solution of Cu^{2+} ions and (b) FTIR spectra of CDA−silica@ZIF-8/120cy before and after adsorption of Cu^{2+}. Note that all three samples in (a) are aerogels. (c) Adsorption mechanism depicting ion-exchange with Zn, formation of coordination complex of Cu with N atoms of ZIF-8, and electrostatic interactions between hydroxyl groups of CDA-silica and Cu.

materials, such as ZIF-8 (methanol, MeOH) (1.11 mmol g^{-1}), ZIF-8 (dimethylformamide, DMF) (1.27 mmol g^{-1}), ZIF-8 (dimethylsulfoxide, DMSO) (1.48 mmol g^{-1}),[53] and BP@ZIF8-200cy-12 h (1.5 mmol g^{-1}),[43] at a pressure of 1 atm at 35 °C (Fig. 4d).

A pseudo-first order model was adopted to fit the experimental results conducted with high concentrations of CO$_2$. Such a model type is frequently utilized to predict the adsorption behaviors of physical adsorbents such as zeolites, silica, and activated carbon. Details of the model development and rationale discussed in the ESI† ultimately lead to the following equation:

$$q_t = q_e(1 - e^{(-k_f t)}) \qquad (1)$$

where, q_e (mmol g^{-1}) and q_t (mmol g^{-1}) are the CO$_2$ adsorption capacity at equilibrium and at any time respectively for per mass of adsorbent, and k_f (min^{-1}) is the rate constant of first order adsorption.

The saturated adsorption capacity observed in the experiments, as well as the anticipated adsorption capacity derived from the model, along with the calculated kinetic constants, are presented in Table S1.† The experimental results as well as the fitting model are illustrated in Fig. 4e, demonstrating a strong alignment between the data and the pseudo-first order model.

This congruence strongly implies the physisorption mechanism since the pseudo-first-order model is frequently utilized to predict the adsorption behaviors of physical adsorbents. The interaction between CO$_2$ molecules and NFA adsorption sites was investigated using *in situ* FTIR. The IR spectrum of ZIF-8 loaded with CO$_2$ provided evidence for guest–host interactions between the ZIF-8 framework and CO$_2$.[54] In the case of CDA–silica@ZIF8-120cy and CDA–silica@ZIF8-60cy, the adsorption band caused by the asymmetric stretching vibration (V_3 vibration) of CO$_2$ molecules, was observed in the range of 2335–2350 cm^{-1} (Fig. 4f).[55] The results showed that the adsorbent sites were filled with increasing time, and the peaks became stable after about 15 minutes.

2.4 Heavy metal removal

We also assessed the water purification performance of our hybrid aerogels, to illustrate the pivotal and functional role of ZIF-8 when combined with the CDA–silica aerogel matrix. Cu^{2+} stands out as a major heavy metal ion, known for its toxic effects on water bodies and biological systems. Batch adsorption experiments were conducted to measure the hybrid aerogels' maximum adsorption capacity for Cu^{2+} ions. A pH of 5 was maintained in the stock solution containing Cu^{2+} ions (100 mg L^{-1}) to minimize electrostatic repulsion of the aerogel

220 | *J. Mater. Chem. A*, 2024, **12**, 214–226

This journal is © The Royal Society of Chemistry 2024

with Cu^{2+} ions before carrying out the experiments. Such a pH was selected to reduce its influence on the surface charge of the aerogel matrix. At lower pH levels, the increased concentration of H^+ ions in the solution, along with a high degree of protonation of the aerogel surface, leads to competition with Cu^{2+} ions for adsorption into active sites. Conversely, higher pH or alkaline conditions cause the precipitation of cupric hydroxide due to larger content of OH^- ions in the solution.

Fig. 5a depicts the equilibrium adsorption capacity (Q_e) for 20 mg of the adsorbent (aerogel) load after 24 hours. The control CDA–silica aerogel showed a maximum Q_e of 189.7 mg g^{-1} with a removal efficiency of 75%. Upon the integration of ZIF-8, the Q_e increases to 245.9 mg g^{-1} and 248.4 mg g^{-1} for CDA–silica@ZIF8-60cy and CDA–silica@ZIF8-120cy respectively. The removal efficiency, evaluated for ZIF-8 grown using both ALD cycles, consistently exceeded 95%. The sample treated with ZIF-8 grown using 120 cycles of ALD reached a maximum removal efficiency of 99%, giving us a final Cu concentration of 0.62 ± 0.16 mg L^{-1}, which is within the standard set by both Environmental Protection Agency (EPA) at 1.3 mg L^{-1} and 2.0 mg L^{-1} by World Health Organization (WHO).[56] Table S2† presents a comparison between our study and other recent research that focuses on the removal of copper (Cu) using composites based on ZIF-8. Our work demonstrates a high and comparable maximum adsorption capacity (Q_e) when compared to these studies and it's important to note that we achieved this

without even optimizing our approach. Moreover, these studies employed a solvothermal technique for ZIF-8 synthesis which is not environmentally desirable.

Zeta potential measurements reveal that the surface of the CDA–silica (ζ-potential of -19.9 ± 0.72 mV) and CDA–silica@ZIF-8 (ζ-potential of -4.32 ± 0.22 mV) is negatively charged at pH 5. This facilitates an increased electrostatic attraction with Cu^{2+} ions. The presence of a large number of hydroxyl groups in CDA–silica offers many active sites and thus helps in the adsorption of Cu^{2+}.[35] To probe further, the adsorption mechanism was studied through FTIR analysis. As inferred from Fig. 5b, the FTIR spectra before adsorption show the characteristic peaks of C=N, C–N, out-of-plane bending of 2-MeIm in ZIF-8 at 1580, 1146, 755, and 420 cm^{-1} respectively. However, after adsorption, the peaks corresponding to C–H, C–N, and the out-of-plane bending of 2-MeIm decreased in intensity. This indicates the formation of coordination bonds between Cu and N atoms on 2-MeIm. The Zn–N peak intensity also decreased after adsorption, revealing possible ion-exchange between Zn^{2+} and Cu^{2+}. Based on all the evidence, we postulate that the adsorption of Cu^{2+} on the hybrid NFA occurs *via* a combination of electrostatic attraction, ion exchange, and the formation of a coordination complex with N atoms as depicted in Fig. 5c.[56] The ZIF-8 works in concert with the aerogels to provide a framework with tunable pore size, hierarchical porosity, and abundant functional groups,
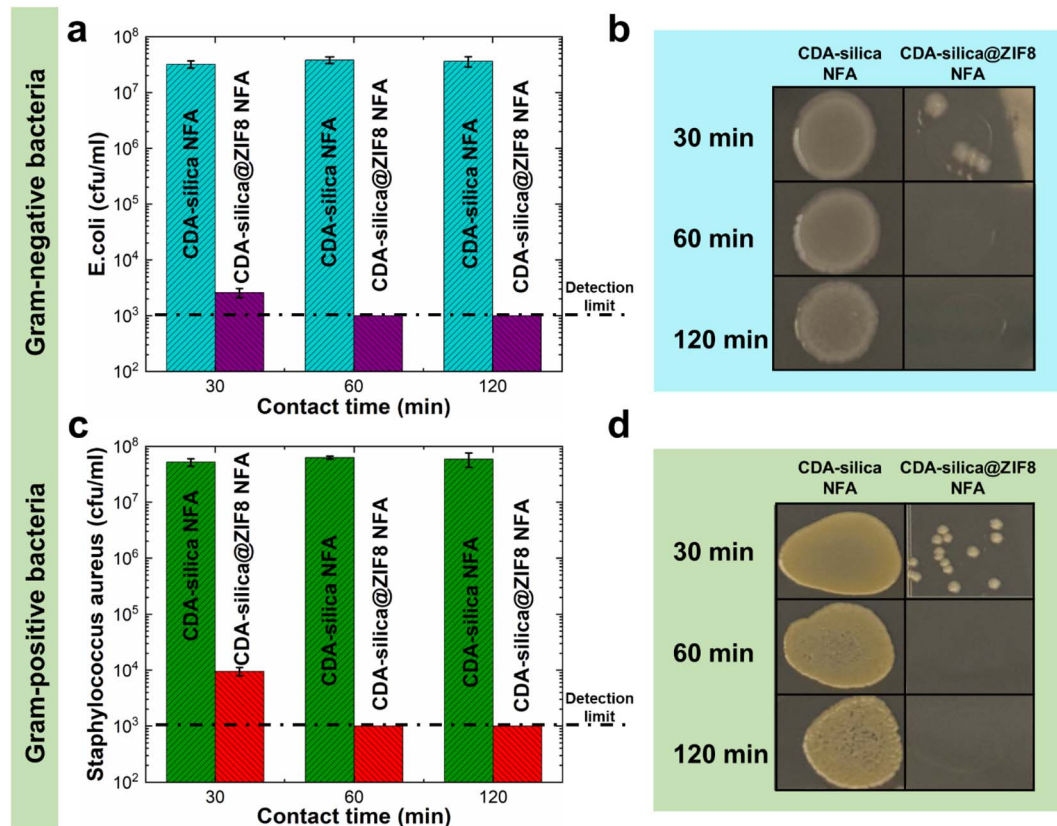

Fig. 6 Antimicrobial properties of CDA–silica@ZIF8-120cy NFA against (a and b) Gram-negative (*E. coli*) and (c and d) Gram-positive (*S. aureus*) bacteria.

This journal is © The Royal Society of Chemistry 2024

J. Mater. Chem. A, 2024, **12**, 214–226 | **221**

facilitating strong binding sites for Cu^{2+} and enhanced the adsorption capacity. The mechanically stable and resilient nature for CDA–silica@ZIF-8 aerogel would further facilitate heavy metal ion adsorption without compromising structural integrity.

2.5 Antibacterial properties

Infectious diseases are a significant public health concern, causing global social and economic disruption. Pathogenic bacteria such as *Escherichia coli* (*E. coli*), *Salmonella enterica*, and others can cause severe illness.[57,58] ZIF-8 has been recently recognized as an antimicrobial agent due to its capability to release zinc ions, which have been shown to have potential antimicrobial activity.[43,59–61] Metal ions exert their microorganism (bacteria and fungi) growth inhibition through the generation of hydroxyl and superoxide anion free radicals through oxidation.[62] Alternatively, a series of redox reactions can lead to cell death by impacting critical cell structures (cell wall, cell membrane, DNA, *etc.*) and metabolic pathways.[63] The high porosity and uniform synthesis of ZIF-8 crystals on CDA–silica nanofibers in the hierarchical porous structure of the NFA enable CDA–silica@ZIF-8 hybrid NFA to exhibit efficient antimicrobial properties with increased accessibility to bacteria. We evaluated the antibacterial performance of CDA–silica@ZIF8-120cy NFA using bioassays with both Gram-negative (*E. coli*) and Gram-positive (*Staphylococcus aureus*, *S. aureus*) bacteria. The results illustrated in Fig. 6 revealed that after 30, 60, and 120 min of incubation with both bacteria, the pristine CDA–silica NFA displayed poor antibacterial activity. In contrast, CDA–silica@ZIF8-120cy NFA showed an antibacterial rate of 100% after 1 and 2 h of incubation with *E. coli* (Fig. 6a and b), and *S. aureus* (Fig. 6c and d). Alternatively, CDA–silica@ZIF8-120cy NFA showed a minimum of 4.47 log 10 reduction of *E. coli* and *S. aureus* after 1 h of incubation, while CDA–silica NFA displayed no microbial reduction as listed in Table 1. It is worth mentioning that the detection limit of the antibacterial contact assay is 10^3 cfu mL^{-1}, which explains the similar values for $\log_{10}$ reduction observed after 60 and 120 min as they are below this limit. Details on the analysis are presented in the Antibacterial contact assays section. The antibacterial efficiency of ZIF-8 is believed to be a result of the combination of the surface effect of zinc ions and physical contact with the bacteria. Additionally, the enhanced efficiency of our CDA–silica@ZIF8-120cy composite can be attributed to the uniformly coated and more accessible ZIF-8 from various sites of the hierarchically porous NFA. While these initial studies demonstrate the ability of CDA–silica@ZIF8-120cy NFA to inhibit bacterial growth,

a detailed investigation of the functional attributes of the MOF hybrid NFAs can generate functional products that can be utilized in various applications, such as the development of membranes for removal of waterborne pathogens or for creation of antimicrobial membranes to interrupt the spread of waterborne pathogens, which has become a global concern.

3. Conclusions

This study presents a straightforward approach to synthesize MOF-based hybrid NFAs with enhanced functionality. We successfully integrated ZIF-8, a subclass of MOFs, onto a 3D structured hierarchically porous CDA–silica nanofibrous aerogel (NFA). The synthesis involved depositing thin layers of ZnO *via* ALD on the NFA substrate, followed by vapor phase conversion of ZnO to ZIF-8 using 2-MeIm as an organic linker vapor. The resulting CDA–silica@ZIF-8 NFA exhibited remarkable properties suitable for diverse applications. The hierarchical cellular structure and high specific surface area provided by the nanofibrous architecture, combined with the micro/mesoporosity of ZIF-8 crystals, led to efficient CO_2 adsorption with rapid kinetics. The hybrid NFA also demonstrated excellent antibacterial properties against both Gram-negative and Gram-positive bacteria due to the presence of ZIF-8 and its antimicrobial zinc ions. Moreover, the material exhibited exceptional performance in the removal of heavy metal ions, particularly copper (Cu(II)), making it a potential candidate for water purification applications. The mechanically robust nature of the aerogel, withstanding large deformations without collapse, further enhances its applications in various fields. The unique combination of properties, including ultralight weight, hierarchical porosity, and mechanical resilience, makes the CDA–silica@ZIF-8 NFA a promising and versatile platform for applications in sorption, catalysis, filtration, and antimicrobial air filters. Our study highlights the potential of MOF-based hybrid nanofibrous aerogels as sustainable and scalable materials with superior functionality in various domains.

4. Experimental section

4.1 Materials

2-MeIm (99%) and zinc nitrate hexahydrate (98%) were obtained from Acros Organics. Cellulose diacetate (CDA, acetyl: 39.8% and hydroxyl: 3.5%) was supplied by Eastman Chemicals. Tetraethyl orthosilicate (TEOS, 99.8%), *N,N*-dimethylformamide (DMF, 99.9%), dimethylacetamide (DMAC), acetone (99%), hydrochloric acid (HCl, 37%) and isopropanol (>99.5%) were obtained from Sigma-Aldrich. Anhydrous tertiary butanol (*t*-BuOH, 99+%) was purchased from Alfa Aesar. Diethylzinc (DEZ, 95%) was obtained from STREM Chemicals, Inc.

4.2 Sol–gel electrospinning of CDA–silica nanofibers

Cellulose diacetate (CDA) solution (11 wt%) was prepared by stirring CDA in a cosolvent of DMAC/acetone (1 : 2 weight ratio) for an extended period. Silica precursor mixture was prepared by mixing TEOS, DMF, H_2O, and HCl in a molar ratio of 1 : 10 :

Table 1 Logarithmic (log 10) reduction values of microbial loading measured with *E. coli* and *S. aureus* contacted with CDA–silica@ZIF8-120cy NFA

	30 min	60 min	120 min
E. coli $\log_{10}$ reduction	4.06	>4.47	>4.47
S. aureus $\log_{10}$ reduction	3.50	>4.47	>4.47

222 | *J. Mater. Chem. A*, 2024, **12**, 214–226

This journal is © The Royal Society of Chemistry 2024

18.75 : 0.021 and the resulting solution was subjected to magnetic stirring at 70 °C for one hour. The silica precursor mixture was then gradually added to the CDA solution in a weight ratio of 1 : 4 and the mixture was further stirred for an additional hour at 70 °C. Electrospinning was subsequently performed by loading the mixture of silica precursor and CDA solution into a 10 mL syringe fitted with a 22 G metal needle and spinning at a controlled feed rate of 0.5 mL h^{-1}. A high voltage of 20 kV was applied, with a constant tip-to-collector distance of 15 cm. The resultant fibers were collected in the form of a nonwoven membrane on an aluminum foil wrapped around a metallic collector connected to a grounded electrode. The temperature and humidity during electrospinning were maintained at 21 ± 4 °C and 21 ± 2%, respectively.[35]

4.3 NFA fabrication

CDA–silica NFA was synthesized *via* freeze-drying of short nanofiber dispersions in *t*-BuOH. 135 mg of CDA–silica nanofiber mats were cut into 1 × 1 cm^2 pieces. To achieve a stable dispersion, the nanofiber mats were homogenized with 20 mL of *t*-BuOH for 15 minutes at 12 000 rpm using an IKA T25 homogenizer. The resulting dispersion was then poured into a glass beaker and frozen in a mixture of dry ice and 2-propanol for 20 minutes. The frozen mixture was then freeze-dried in a Labconco FreeZone 6L freeze-drying system at ~0.003 mbar and −85 °C for 48 hours to obtain CDA–silica hybrid nanofibrous aerogel. Finally, the NFA were thermally treated at 180 °C for 2 hours, followed by an additional hour at 240 °C in a vacuum oven.[35]

4.4 ZnO ALD on CDA–silica nanofibers and NFA substrates

Thin layers of zinc oxide (ZnO) were coated on CDA–silica nanofibers and NFA substrate using a home-built hot-wall viscous-flow ALD reactor.[15,43,64] Nitrogen (N$_2$) was utilized as the purge and carrier gas during the deposition process, which was conducted at a temperature of 90 °C and a pressure of 1.1–1.2 torr. The deposition recipe consisted of four steps: 1s/40s/1s/40s corresponding to DEZ dose/N$_2$ purge/H$_2$O dose/N$_2$ purge. The growth rate of ZnO was monitored by measuring the film thickness on silicon with native oxide (~2 nm) using J. A. Woollam alpha-spectroscopic ellipsometer (SE) at an incidence angle of 70°. The results revealed a growth rate of approximately 1.7 Å per cycle (10 nm after 60 cycles) was obtained.

4.5 Vapor phase synthesis of ZIF-8 on ZnO coated CDA–silica NFA

The conversion of ZnO to ZIF-8 was performed by utilizing ZnO coated CDA–silica NFA substrates. The NFA substrates were suspended using a string in a closed glass jar containing a powder bed of 2-MeIm (1 g) to avoid direct contact between the substrate and the powder bed. The substrates were suspended 1 cm above the 2-MeIm powder bed. The conversion process was conducted at a temperature of 135 °C for 6 hours. The samples are labeled as CDA–silica@ZIF8-*X*cy, indicating that they are CDA–silica@ZIF-8 hybrid NFA that have undergone *X* cycles of ZnO ALD treatment. Note that details on the

vapor phase synthesis of MOFs have been previously studied and well-documented in the literature.[40–42] This has not been our focus as our primary interest is on using the vapor phase synthesis to create MOF on NFA for enhanced performance of MOF, something that has not been attempted before, to the best of our knowledge.

4.6 CO$_2$ adsorption

TA instruments SDT 650 was used to investigate the CO$_2$ adsorption capacity of the CDA–silica@ZIF-8 NFA at various temperatures (35 °C, 60 °C, and 80 °C). A sample weighing between 5–10 mg was heated to 200 °C at a rate of 20 °C min^{-1} under Ar (99.999%) with a flow rate of 150 mL min^{-1} and left for 120 min to eliminate any adsorbed species. The sample was then held at this temperature for 120 minutes to remove any previously adsorbed species. After cooling to the desired analysis temperature, the samples were allowed to equilibrate for 60 minutes before switching the gas flow to a mixture of 15% CO$_2$ and 85% Ar, with a flow rate of 150 mL min^{-1}, for 10 minutes. The cyclic stability experiments were performed using a similar procedure for 50 cycles. Additional experiments were conducted to assess the adsorption of CO$_2$ at higher concentrations (90% CO$_2$ and 10% Ar) at 35 °C and 1 bar. The testing procedure for this experiment was similar to that of the CO$_2$ adsorption experiment performed at different temperatures.

The interaction between CO$_2$ molecules and adsorption sites in the CDA–silica@ZIF-8 NFA was investigated using *in situ* FTIR. Thermo Fisher Nicolet iS50 FTIR, which was equipped with a DiffusIR sample chamber from Pike Technologies was employed for this analysis. The procedure was conducted by loading the sample into the *in situ* cell and subjecting it to Ar gas purging at 200 °C for 30 minutes. Subsequently, the sample was cooled down to a temperature of 25 °C. In order to acquire the background spectrum, the instrument recorded the spectrum within an Ar stream at 25 °C, which was subsequently automatically subtracted from the sample spectrum. CO$_2$ gas was then introduced into the reaction cell at a flow rate of 40 mL min^{-1}, and spectra were collected iteratively until the spectral curve reached a stabilized state.

4.7 Heavy metal removal

The NFAs were subjected to testing to study their adsorption performance for heavy metal ions. Copper ions (Cu^{2+}) were specifically chosen as the element of interest to investigate the adsorption characteristics. First, a stock solution of 100 mg L^{-1} containing Cu^{2+} ions was prepared by dissolving copper sulfate in DI water and the pH was adjusted to 5 by using 0.1 M NaOH. Different quantities of aerogels were then placed into 50 mL of Cu^{2+} ions aqueous solution which was then subjected to agitation in an orbital shaker at 150 rpm for 24 hours at 25 °C. The resulting supernatant was passed through a 0.45 μm syringe filter. Finally, Inductively Coupled Plasma Optical Emission Spectroscopy (ICP-OES) was used to measure the concentration of Cu^{2+} in the filtrate. The obtained data was used to calculate the adsorption capacity (Q_e, mg g^{-1}) of the aerogels. All experiments were carried out in triplicates.

This journal is © The Royal Society of Chemistry 2024

J. Mater. Chem. A, 2024, **12**, 214–226 | **223**

The adsorption capacity of the aerogels per unit mass and removal efficiency were calculated using the following formulae.

$$Q_e = (C_o - C_e) \times \frac{V}{m} \tag{2}$$

$$R = \frac{(C_o - C_e)}{C_o} \times 100\% \tag{3}$$

C_o (mg L^{-1}) and C_e (mg L^{-1}) are the initial and final concentration of Cu^{2+} ions, V (mL) is the volume of the suspension, m (g) is the mass of the sorbent.

Zeta potential analysis. The zeta potential of the diluted dispersions (0.01 wt%) at pH 5 for the control and CDA–silica@ZIF-8 aerogels was measured using Zetasizer Nano ZSP by Malvern Instruments which consisted of 5 runs each at 25 °C.

4.8 Antibacterial contact assays

The antibacterial activity of CDA–silica and CDA–silica@ZIF-8 NFA were investigated using *Escherichia coli* (*E. coli*, ATCC 8739) and *Staphylococcus aureus* (*S. aureus*, ATCC 6538P) cells as a model microorganism. The *E. coli* cells were grown in a growth media composed of 3.0 grams of beef extract, 5.0 grams of peptone, and 1 liter of deionized water (DI) for 4 hours. The cell suspension was then centrifuged at 4000 × g for 5 minutes and resuspended in phosphate-buffered saline (PBS). The optical density of the *E. coli* suspension was quantified using a Shimadzu UV-1800 spectrophotometer and adjusted to a final OD$_{600}$ nm equal to 0.4. 20 mg of CDA–silica and CDA–silica@ZIF-8 NFA were placed in well plates and wetted with 10 µL of the *E. coli* suspension. A piece of polyethylene was gently placed on top of the samples. The samples were incubated at 37 °C in the dark for 1, 3, 8 and 24 hours. They were then removed, washed with 90 µL of neutralizing buffer, and serially diluted. Dilutions were deposited on top of agar plates and incubated for 18 hours at 37 °C. The final bacteria concentration was determined as the number of colonies per mL. A similar procedure was conducted to estimate the number of bacterial colonies after storing the control samples at 37 °C for 1, 3, 8 and 24 hours without CDA–silica and CDA–silica@ZIF-8 NFA. All experiments were conducted in triplicate. The antibacterial rate (% AR) of the samples was determined by using the following formula:

$$\% \text{ AR} = \left(1 - \left(\frac{\text{CFU of sample}}{\text{CFU of control}}\right)\right) \times 100 \tag{4}$$

where CFU stands for colony forming unit.[65,66] The detection limit for the antibacterial contact assay is 10^3 cfu mL^{-1}. The values in Table 1 was calculated by taking the log 10 of initial bacteria concentration minus log 10 after x minutes. The initial concentration for *E. coli* and *S. aureus* are 3×10^7 and 6×10^7 respectively.

Conflicts of interest

The authors declare no conflict of interest.

Acknowledgements

References

1 H. Furukawa, K. E. Cordova, M. O'Keeffe and O. M. Yaghi, *Science*, 2013, **341**(6149), 1230444.

2 X. Jia, M. Peydayesh, Q. Huang and R. Mezzenga, *Small*, 2022, **18**, 2105502.

3 P. Horcajada, R. Gref, T. Baati, P. K. Allan, G. Maurin, P. Couvreur, G. Férey, R. E. Morris and C. Serre, *Chem. Rev.*, 2012, **112**, 1232–1268.

4 B. Seoane, J. Coronas, I. Gascon, M. E. Benavides, O. Karvan, J. Caro, F. Kapteijn and J. Gascon, *Chem. Soc. Rev.*, 2015, **44**, 2421–2454.

5 M. S. Denny, J. C. Moreton, L. Benz and S. M. Cohen, *Nat. Rev. Mater.*, 2016, **1**, 16078.

6 E. A. Dolgopolova, A. M. Rice, C. R. Martin and N. B. Shustova, *Chem. Soc. Rev.*, 2018, **47**, 4710–4728.

7 C. Liu, Y. Bai, W. Li, F. Yang, G. Zhang and H. Pang, *Angew. Chem. Int. Ed.*, 2022, **61**, e2021162.

8 G. Liu, V. Chernikova, Y. Liu, K. Zhang, Y. Belmabkhout, O. Shekhah, C. Zhang, S. Yi, M. Eddaoudi and W. J. Koros, *Nat. Mater.*, 2018, **17**, 283–289.

9 L. Zhu, L. Zong, X. Wu, M. Li, H. Wang, J. You and C. Li, *ACS Nano*, 2018, **12**, 4462–4468.

10 G. W. Peterson, D. T. Lee, H. F. Barton, T. H. Epps and G. N. Parsons, *Nat. Rev. Mater.*, 2021, **6**, 605–621.

11 S. Furukawa, J. Reboul, S. Diring, K. Sumida and S. Kitagawa, *Chem. Soc. Rev.*, 2014, **43**, 5700–5734.

12 Y. Ma, Z. Dong, M. You, Y. Zhang, X. Feng, X. Ma and J. Meng, *Chem. Commun.*, 2019, **55**, 10146–10149.

13 M. Kalaj and S. M. Cohen, *Angew. Chem., Int. Ed.*, 2020, **59**, 13984–13989.

14 J. Zhao, D. T. Lee, R. W. Yaga, M. G. Hall, H. F. Barton, I. R. Woodward, C. J. Oldham, H. J. Walls, G. W. Peterson and G. N. Parsons, *Angew. Chem.*, 2016, **128**, 13418–13422.

15 D. T. Lee, J. Zhao, C. J. Oldham, G. W. Peterson and G. N. Parsons, *ACS Appl. Mater. Interfaces*, 2017, **9**, 44847–44855.

16 M. Kalaj, M. S. Denny, K. C. Bentz, J. M. Palomba and S. M. Cohen, *Angew. Chem.*, 2019, **131**, 2358–2362.

17 Y. Deng, Y. Wang, X. Xiao, B. J. Saucedo, Z. Zhu, M. Xie, X. Xu, K. Yao, Y. Zhai, Z. Zhang and J. Chen, *Small*, 2022, **18**, 2202928.

18 T. Kitao, Y. Zhang, S. Kitagawa, B. Wang and T. Uemura, *Chem. Soc. Rev.*, 2017, **46**, 3108–3133.

19 A. J. Brown, N. A. Brunelli, K. Eum, F. Rashidi, J. R. Johnson, W. J. Koros, C. W. Jones and S. Nair, *Science*, 2014, **345**, 72–75.

20 Y. Dou, W. Zhang and A. Kaiser, *Adv. Sci.*, 2020, **7**, 1902590.

21 Q. Qian, P. A. Asinger, M. J. Lee, G. Han, K. M. Rodriguez, S. Lin, F. M. Benedetti, A. X. Wu, W. S. Chi and Z. P. Smith, *Chem. Rev.*, 2020, **120**, 8161–8266.

22 M. Matsumoto and T. Kitaoka, *Adv. Mater.*, 2016, **28**, 1765–1769.

23 V. Rahmanian, T. Pirzada, S. Wang and S. A. Khan, *Adv. Mater.*, 2021, **33**, 2102892.

24 H. Zhu, X. Yang, E. D. Cranston and S. Zhu, *Adv. Mater.*, 2016, **28**, 7652–7657.

25 J. Rostami, T. Benselfelt, L. Maddalena, C. Avci, F. A. Sellman, G. C. Ciftci, P. A. Larsson, F. Carosio, F. Akhtar, W. Tian and L. Wågberg, *Adv. Mater.*, 2022, **34**, 2204800.

26 C. Tan, M. C. Lee, M. Arshadi, M. Azizi and A. Abbaspourrad, *Angew. Chem., Int. Ed.*, 2020, **59**, 9506–9513.

27 J. Wang, J. Yang, H. Zhu, B.-G. Li and S. Zhu, *Chem. Eng. J.*, 2023, **456**, 141026.

28 J. Rostami, K. Gordeyeva, T. Benselfelt, E. Lahchaichi, S. A. Hall, A. V. Riazanova, P. A. Larsson, G. C. Ciftci and L. Wågberg, *Mater. Today*, 2021, **48**, 47–58.

29 X. Ma, Y. Lou, X.-B. Chen, Z. Shi and Y. Xu, *Chem. Eng. J.*, 2019, **356**, 227–235.

30 Y. Fei, M. Liang, L. Yan, Y. Chen and H. Zou, *Chem. Eng. J.*, 2020, **392**, 124815.

31 P. K. Chattopadhyay and N. R. Singha, *Coord. Chem. Rev.*, 2021, **446**, 214125.

32 L. Wang, H. Xu, J. Gao, J. Yao and Q. Zhang, *Coord. Chem. Rev.*, 2019, **398**, 213016.

33 F. Deuber and C. Adlhart, *Chimia*, 2017, **71**, 236.

34 Y. Si, J. Yu, X. Tang, J. Ge and B. Ding, *Nat. Commun.*, 2014, **5**, 5802.

35 T. Pirzada, Z. Ashrafi, W. Xie and S. A. Khan, *Adv. Funct. Mater.*, 2020, **30**, 1907359.

36 Y. Si, Q. Fu, X. Wang, J. Zhu, J. Yu, G. Sun and B. Ding, *ACS Nano*, 2015, **9**, 3791–3799.

37 V. Rahmanian, T. Pirzada, E. Barbieri, S Iftikhar, F. Li and S. A. Khan, *Appl. Mater. Today*, 2023, **32**, 101784.

38 F. Deuber, S. Mousavi, L. Federer, M. Hofer and C. Adlhart, *ACS Appl. Mater. Interfaces*, 2018, **10**, 9069–9076.

39 T. Pirzada, V. Rahmanian and S. A. Khan, in *Applications of Polymer Nanofibers*, Wiley, 2022, pp. 345–371.

40 S. Han and C. B. Mullins, *ChemSusChem*, 2020, **13**, 5433–5442.

41 I. Stassen, N. Campagnol, J. Fransaer, P. Vereecken, D. De Vos and R. Ameloot, *CrystEngComm*, 2013, **15**, 9308.

42 I. Stassen, D. De Vos and R. Ameloot, *Chem.–Eur. J.*, 2016, **22**, 14452–14460.

43 S. Wang, T. Pirzada, W. Xie, E. Barbieri, O. Hossain, C. H. Opperman, L. Pal, Q. Wei, G. N. Parsons and S. A. Khan, *Appl. Mater. Today*, 2022, **28**, 101517.

44 K. He, N. Chen, C. Wang, L. Wei and J. Chen, *Cryst. Res. Technol.*, 2018, **53**, 1700157.

45 S. Zhong, Q. Wang and D. Cao, *Sci. Rep.*, 2016, **6**, 21295.

46 A. Gu, J. Chen, Q. Gao, M. M. Khan, P. Wang, Y. Jiao, Z. Zhang, Y. Liu and Y. Yang, *Appl. Surf. Sci.*, 2020, **516**, 146160.

47 Y.-C. Lou, S.-C. Qi, D.-M. Xue, C. Gu, R. Zhou, X.-Q. Liu and L.-B. Sun, *Chem. Eng. J.*, 2020, **399**, 125845.

48 S.-C. Qi, X.-J. Lu, Y.-C. Lou, R. Zhou, D.-M. Xue, X.-Q. Liu and L.-B. Sun, *Engineering*, 2022, **16**, 154–161.

49 D. Y. C. Leung, G. Caramanna and M. M. Maroto-Valer, *Renewable Sustainable Energy Rev.*, 2014, **39**, 426–443.

50 M. Bui, C. S. Adjiman, A. Bardow, E. J. Anthony, A. Boston, S. Brown, P. S. Fennell, S. Fuss, A. Galindo, L. A. Hackett, J. P. Hallett, H. J. Herzog, G. Jackson, J. Kemper, S. Krevor, G. C. Maitland, M. Matuszewski, I. S. Metcalfe, C. Petit, G. Puxty, J. Reimer, D. M. Reiner, E. S. Rubin, S. A. Scott, N. Shah, B. Smit, J. P. M. Trusler, P. Webley, J. Wilcox and N. M. Dowell, *Energy Environ. Sci.*, 2018, **11**, 1062–1176.

51 X. Gong, Y. Wang and T. Kuang, *ACS Sustain. Chem. Eng.*, 2017, **5**, 11204–11214.

52 K. Díaz, L. Garrido, M. López-González, L. F. del Castillo and E. Riande, *Macromolecules*, 2010, **43**, 316–325.

53 Y. Guan, J. Shi, M. Xia, J. Zhang, Z. Pang, A. Marchetti, X. Wang, J. Cai and X. Kong, *Appl. Surf. Sci.*, 2017, **423**, 349–353.

54 Y. Hu, Z. Liu, J. Xu, Y. Huang and Y. Song, *J. Am. Chem. Soc.*, 2013, **135**, 9287–9290.

55 S. Bordiga, L. Regli, F. Bonino, E. Groppo, C. Lamberti, B. Xiao, P. S. Wheatley, R. E. Morris and A. Zecchina, *Phys. Chem. Chem. Phys.*, 2007, **9**, 2676.

56 N. Bakhtiari, S. Azizian, S. M. Alshehri, N. L. Torad, V. Malgras and Y. Yamauchi, *Microporous Mesoporous Mater.*, 2015, **217**, 173–177.

57 A. K. Jha and K. Prasad, *Biotechnol. J.*, 2010, **5**, 285–291.

58 F. Wang, Y. Si, J. Yu and B. Ding, *Adv. Funct. Mater.*, 2021, **31**, 2107223.

59 Z. Liang, H. Wang, K. Zhang, G. Ma, L. Zhu, L. Zhou and B. Yan, *Chem. Eng. J.*, 2022, **428**, 131349.

60 R. Li, T. Chen and X. Pan, *ACS Nano*, 2021, **15**, 3808–3848.

61 M. Taheri, D. Ashok, T. Sen, T. G. Enge, N. K. Verma, A. Tricoli, A. Lowe, D. R. Nisbet and T. Tsuzuki, *Chem. Eng. J.*, 2021, **413**, 127511.

62 W.-J. Chen, P.-J. Tsai and Y.-C. Chen, *Small*, 2008, **4**, 485–491.

63 C. López de Dicastillo, M. G. Correa, F. B. Martínez, C. Streitt and M. J. Galotto, in *Antimicrobial Resistance - A One Health Perspective*, IntechOpen, 2021.

64 J. Zhao, B. Gong, W. T. Nunn, P. C. Lemaire, E. C. Stevens, F. I. Sidi, P. S. Williams, C. J. Oldham, H. J. Walls,

This journal is © The Royal Society of Chemistry 2024

J. Mater. Chem. A, 2024, **12**, 214–226 | 225

S. D. Shepherd, M. A. Browe, G. W. Peterson, M. D. Losego and G. N. Parsons, *J. Mater. Chem. A*, 2015, **3**, 1458–1464.

65 M. Su, R. Zhang, J. Li, X. Jin, X. Zhang and D. Qin, *Cellulose*, 2021, **28**, 11713–11727.

66 C. L. de Dicastillo, C. Patiño, M. J. Galotto, Y. Vásquez-Martínez, C. Torrent, D. Alburquenque, A. Pereira and J. Escrig, *Beilstein J. Nanotechnol.*, 2019, **10**, 1716–1725.

226 | *J. Mater. Chem. A*, 2024, **12**, 214–226

This journal is © The Royal Society of Chemistry 2024